

LiDAR Data Synthesis with Denoising Diffusion Probabilistic Models

Kazuto Nakashima¹ and Ryo Kurazume¹

Abstract—Generative modeling of 3D LiDAR data is an emerging task with promising applications for autonomous mobile robots, such as scalable simulation, scene manipulation, and sparse-to-dense completion of LiDAR point clouds. Existing approaches have shown the feasibility of image-based LiDAR data generation using deep generative models while still struggling with the fidelity of generated data and training instability. In this work, we present R2DM, a novel generative model for LiDAR data that can generate diverse and high-fidelity 3D scene point clouds based on the image representation of range and reflectance intensity. Our method is based on the denoising diffusion probabilistic models (DDPMs), which have demonstrated impressive results among generative model frameworks and have been significantly progressing in recent years. To effectively train DDPMs on the LiDAR domain, we first conduct an in-depth analysis regarding data representation, training objective, and spatial inductive bias. Based on our designed model R2DM, we also introduce a flexible LiDAR completion pipeline using the powerful properties of DDPMs. We demonstrate that our method outperforms the baselines on the generation task of KITTI-360 and KITTI-Raw datasets and the upsampling task of KITTI-360 datasets. Our code and pre-trained weights will be available at <https://github.com/kazuto1011/r2dm>.

I. INTRODUCTION

LiDAR (light detection and ranging) sensors play a pivotal role in empowering mobile robots with the ability to perceive the surrounding obstacles and geometry for autonomous navigation and mapping. The sensors produce accurate 3D point clouds by emitting laser beams at omnidirectional angles and detecting reflections from objects. The collected point clouds can be used for 3D scene understanding, such as semantic segmentation [1] and object detection.

However, high-density and high-quality point clouds are not easily accessible on all platforms. For instance, LiDAR sensors with a high number of beams are generally expensive. Therefore, the low-cost yet low-beam LiDAR sensors can be a practical option for system development, although they suffer from a degradation of scene perception due to the sparsity of the point clouds.

Generative modeling of LiDAR point clouds is a frontier approach to tackle these issues [2]–[5], which aims to learn the prior distribution of 3D scenes. The sparse or incomplete point clouds can be restored by using the learned priors. Motivated by the impressive achievements of deep generative models, various kinds of approaches have been proposed for LiDAR data generation, such as variational autoencoders

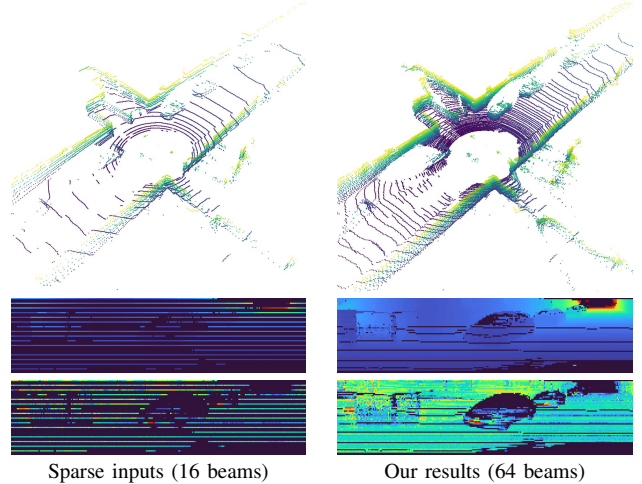


Fig. 1. **LiDAR upsampling using our diffusion model.** We show the sparse LiDAR inputs and our upsampled results as point clouds (top), range images (middle), and reflectance images (bottom). Our results were obtained through image-based conditional generation using our model. The range and reflectance images are partially zoomed for visual purposes.

(VAEs) [2], generative adversarial networks (GANs) [2]–[4], and energy-based generative models (EBMs) [5].

In this paper, we present R2DM, a generative model for LiDAR data generation that can generate diverse and high-fidelity 3D scene point clouds. As a framework for building a generative model, we employ denoising diffusion probabilistic models (DDPMs) [6], which have significantly progressed in recent years. DDPMs offer various benefits over other frameworks such as training stability, computational parallelizability, and sample quality, as demonstrated in a wide range of domains [6]–[8].

Similar to the relevant studies [2]–[5], we cast our task as an image-based generation, where LiDAR point clouds are represented by equirectangular images where each pixel contains pointwise range and reflectance information. To demonstrate the effectiveness of DDPM in the LiDAR domain, we first conducted an in-depth analysis of model configuration, focusing on three aspects: data representation, training objectives, and spatial inductive bias. We find that incorporating spatial inductive bias is critical for enhancing the performance. Our designed R2DM architecture achieves state-of-the-art generation performance across various metrics including point clouds, range images, and bird’s eye views. Furthermore, our R2DM can also be applied to LiDAR completion tasks. We propose a flexible pipeline capable of handling various types of corruption, including issues stemming from low-beam LiDAR configurations. R2DM

*This work was supported by JSPS KAKENHI Grant Number JP23K16974 and JST [Moonshot R&D] [Grant Number JPMJMS2032]

¹Kazuto Nakashima and Ryo Kurazume are with the Faculty of Information Science and Electrical Engineering, Kyushu University, Japan. {k.nakashima, kurazume}@ait.kyushu-u.ac.jp

outperforms the baseline in the beam-level upsampling task.

Our contributions can be summarized as follows:

- We present R2DM, a denoising diffusion probabilistic model (DDPM) for LiDAR data, capable of generating diverse and high-fidelity range images with a reflectance modality. Our R2DM outperforms the existing baselines on the KITTI-360 [9] and KITTI-Raw [10] datasets.
- We provide an in-depth analysis to effectively train DDPMs on the LiDAR domain. Our key finding is that an explicit spatial bias significantly influences geometrically consistent generation.
- We introduce a flexible LiDAR completion pipeline using powerful properties offered by DDPMs (see Fig. 1 for instance), which also outperforms the baseline on the KITTI-360 upsampling task.

II. RELATED WORK

A. Generative Models

Generative models aim to learn the underlying distribution of a dataset. During the last decade, the rapid advancements in deep neural networks have spurred the development of various frameworks for generative models.

One of the most prominent frameworks is generative adversarial networks (GANs) [11]. A GAN consists of a generator, which creates data from sampled latent variables, and a discriminator, which distinguishes between the generated and real data. These networks are trained alternately to minimize the adversarial objective. While GANs are known for their sampling efficiency and high synthesis quality, they can experience instability and mode-collapse during training due to the competitive nature of the training objective.

Recently, energy-based models, including score-based generative models [12, 13] and denoising diffusion probabilistic models (DDPM) [6, 7, 14], have garnered substantial attention. These models have several notable advantages that have led to significant advancements, especially in the field of text-to-image generation [7, 15]. Firstly, they offer a simple loss objective and stable training environment thanks to the maximum likelihood estimation-based formulation. This stands in contrast to GANs, which frequently suffer from instability and necessitate extensive training. Secondly, a single model is sufficient to facilitate both the generation and inference processes, unlike other generative models. Moreover, the formulation of the diffusion process as a Markov model allows each denoising step to be fully parallelized, which, in turn, enables scaling of the training data and model capacity.

B. LiDAR Data Generation

Motivated by the progress in the image domain, some studies have reported generative models for LiDAR data.

Caccia *et al.* [2] initiated pivotal work on this subject, utilizing VAEs and GANs to train LiDAR data. Based on the range image-based representation, they effectively showcased the potential for LiDAR data generation. Nakashima and Kurazume [3] noted that the discrete dropout noises present in range images could obstruct the training of GANs,

which consist of continuous functions. To tackle the issue, they introduced DUSTy, a GAN architecture disentangling the noisy range images into denoised range images and the corresponding dropout probabilities. Building upon the foundation of DUSTy, Nakashima *et al.* [4] introduced DUSTy v2, an enhanced version capable of representing LiDAR range images at arbitrary resolutions. This was achieved by formulating the generative process through implicit neural representation.

LiDARGen, proposed by Zyrianov *et al.* [5], is closely related to our work. It is a diffusion-based generative model capable of generating LiDAR data using the range image representation. They employed a noise-conditional score network (NCSN) [13] and customized the model to leverage the LiDAR-specific properties, such as incorporating circulating kernel operations and introducing an angular coordinate input as a spatial bias. LiDARGen has demonstrated state-of-the-art results on standard LiDAR datasets, albeit with only subtle improvements compared to existing GAN approaches.

In this paper, our primary aim is to reconfigure this diffusion-based generation approach using DDPMs to enhance training efficiency and generation fidelity. Although NCSN employed by LiDARGen has been proven that the objective is almost equivalent to the ancestral DDPM [6], the training methodologies and architecture of DDPMs have been rapidly improving and showcased impressive results in other domains [7, 14]. We demonstrate the significant improvement on qualitatively and quantitatively through our experiments in Section IV.

III. PROPOSED METHOD

To explore the effective DDPM design for LiDAR data, this section provides the formulation of DDPMs and introduce some modification regarding data representation, loss function, and spatial inductive bias. Lastly, we also introduce the LiDAR completion pipeline using our DDPM.

A. Preliminary

In this paper, we employ the DDPM formulated in continuous time $t \in [0, 1]$ [14]. The schematic diagram is depicted in Fig. 2. In DDPM, the inference step is called as the forward diffusion process, which gradually destructs the data sample x by adding noises as evolving the timestep t , as to be the pure Gaussian noise. The training objective of DDPM is *reverse* diffusion process, which is to learn a transition distribution that gradually denoises the Gaussian noise as to be the sampled data x .

Conveniently, the noised samples z_t at timestep t can be given by:

$$q(z_t|x) = \mathcal{N}(\alpha_t x, \sigma_t^2 \mathbf{I}). \quad (1)$$

where α_t and σ_t are parameters to determine the noising schedule. For example, most popular approach is α -cosine schedule where $\alpha_t = \cos(\pi t/2)$ and $\sigma_t = \sin(\pi t/2)$. Note that this process $q(z_t|x)$ is training-free. This transition distribution can be re-parameterized as:

$$z_t = \alpha_t x + \sigma_t \epsilon_t, \text{ where } \epsilon_t \sim \mathcal{N}(0, \mathbf{I}). \quad (2)$$

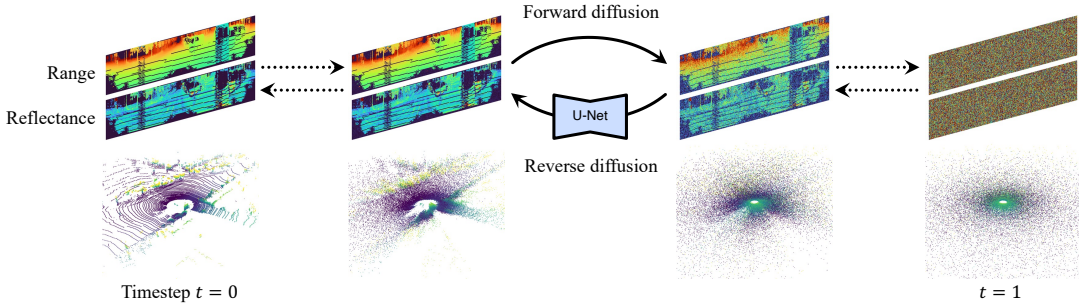


Fig. 2. **Overview of R2DM pipeline.** In R2DM, the U-Net is trained to recursively denoise the intermediate latent variables at $t \leq 1$.

Assuming a variance preserving process as $\alpha_t^2 = 1 - \sigma_t^2$, the transition of latent variables $q(z_t|z_s)$ from timestep s to t , for any $0 \leq s < t \leq 1$, can be written as:

$$q(z_t|z_s) = \mathcal{N}(\alpha_{t|s}z_s, \sigma_{t|s}^2\mathbf{I}). \quad (3)$$

where $\alpha_{t|s} = \alpha_t/\alpha_s$ and $\sigma_{t|s}^2 = \sigma_t - \alpha_{t|s}\sigma_s$. Then, the reverse diffusion process $p(z_s|z_t)$ conditioned by data x is given by:

$$p(z_s|z_t) = q(z_s|z_t, x). \quad (4)$$

The fundamental objective of DDPM is to estimate x at timestep t by neural networks $\hat{x} = x_\theta(z_t)$, where U-Net [6] is generally used. In summary, we first draw z_t by Eq. 2, calculate the error with respect to x , and then denoise the sample z_t into z_s by Eq. 4. In general, predicting noise ϵ_t instead of x is preferable. The loss function is given by:

$$\mathcal{L} = \mathbb{E}_{x, \epsilon \sim \mathcal{N}(0,1), t} [\|\epsilon_t - \epsilon_\theta(z_t, t)\|_2^2], \quad (5)$$

where ϵ_θ is a neural network to be trained. Note that ϵ_θ is conditioned by t for better performance. Then, ϵ_θ is transformed into $\hat{x} = (z_t - \sigma_t\epsilon_\theta(z_t, t))/\alpha_t$. Once the training is complete, we can sample data x by initializing from the Gaussian noise and recursively evaluating $p(z_s|z_t)$ with an arbitrary number of steps T for $t = 1$ to $t = 0$.

B. Data representation

Suppose that a LiDAR sensor has W and H resolution in azimuth and elevation angles respectively and measures a distance d for each angular position. Then range distance d can be projected to a $H \times W$ angular grid by spherical projection. The resultant image has a set of range and reflectance intensity values for each pixel. Following LiDARGen [5], we first convert the depth modality $d \in [0, d_{\max}]^{H \times W}$ into a logarithmic representation $\in [0, 1]^{H \times W}$ as follows:

$$d_{\log} = \frac{\log(d+1)}{\log(d_{\max}+1)}. \quad (6)$$

In this paper, we also compare other popular representations: standard metric depth d and inverse depth $1/d$.

C. Loss function

In Eq. (5), the L_2 loss is used to compute the model prediction. Meanwhile, in the context of monocular depth estimation, Saxena *et al.* [8] found that an L_1 -based formulation offers better performance due to its robustness to

large depth values and noisy holes. In our experiment, we also evaluate the L_1 loss and the combination, the Huber loss.

D. Spatial inductive bias

Each pixel in the initial input of U-Net is *i.i.d.* Gaussian noise, and it does not contain positional information. We consider that structured outputs are achieved through implicit positional encoding by zero padding, as addressed in GAN literature [16, 17]. In our case, many layers are required for the padding information to propagate throughout the entire image due to the horizontally elongated shape (64×1024). Moreover, even padded zero pixels are removed when kernel operations are circulated horizontally. LiDARGen [5] successfully avoids the issue by concatenating angular coordinates (θ, ϕ) to the input of U-Net, motivated by the correlation to geometric structures. We hypothesize that raw angular information alone is insufficient to serve as a spatial bias for U-Net in representing detailed structured images, given its low-frequency component nature. Moreover, raw angular coordinates are unnatural to represent the horizontal cylindrical structure of LiDAR range images.

In this work, we further explore effective coordinates representations. Here, we generalize the inputs as coordinates embedding $\text{CE}(\theta, \phi)$, which is equal to an identity function in the LiDARGen case. We compare two *horizontally-circulated* methods: spherical harmonics [18, 19] and Fourier features [20]. Spherical harmonics represent functions on a sphere through a series of orthogonal functions, which has been used for encoding view directions in neural radiance fields (NeRF) [18]. Similar to Zhang *et al.* [19] on the LiDAR compression task, we encode the angular coordinates inputs by spherical harmonic basis. We compute the embeddings up to the degree of 4. Furthermore, we compare Fourier features [20], originally used in NeRF literature. We employ a \log_2 -spaced scheme used in NeRF [21], which extends the elevation angle and azimuth angle separately to the frequency components of powers of two so that the encoding preserves the cylindrical structure of the angular coordinates.

E. Denoising U-Net

Similar to Saxena *et al.* [8] on monocular depth estimation, our model is built upon Efficient U-Net [7]. We change the input and output channels as to process the 2-channel LiDAR

TABLE I
ARCHITECTURE COMPARISON OF OUR R2DM AND BASELINE

	U-Net architecture	# params	sec/step [†]
LiDARGen [5]	RefineNet [25]	29,694,082	1.508
R2DM (ours)	Efficient U-Net [7]	31,099,650	0.594

[†] 32 samples on the single NVIDIA A6000 GPU

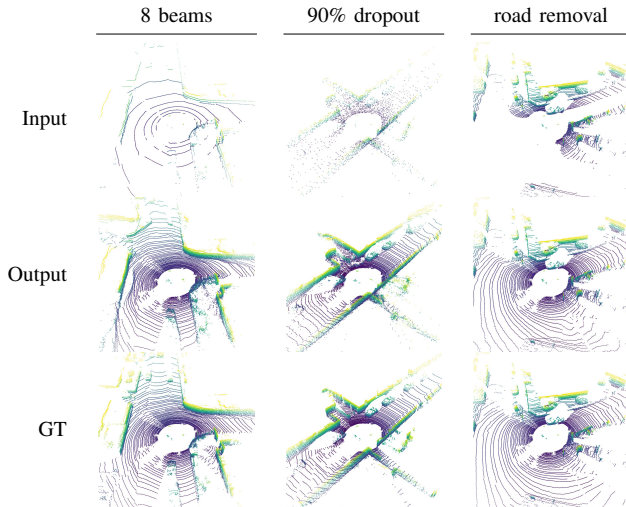


Fig. 3. **Conditional generation using R2DM.** We showcase the simulated corruptions and our restored results. Using the sampling technique recently proposed by RePaint [26], our R2DM can handle the various levels of completion. The road removal mimics the wet road situation.

imagery: depth and reflectance. The continuous timestep t is encoded by a sinusoidal function and injected as affine weights of every adaptive group normalization (AdaGN) layer [22]. We adopt three residual blocks at each resolution and the multi-head self-attention layer at the lowest resolution. The final model involves 31.1M parameters which was adjusted to roughly align with LiDARGen [5] with 29.7M parameters for fair comparison. Table I shows the architecture comparison. All kernel operations, such as convolution and up/down-resampling, are modified to use circular padding in the horizontal direction, as demonstrated in LiDAR processing tasks [3]–[5, 23, 24].

F. Conditional generation

Lugmayr *et al.* [26] proposed RePaint, a DDPM-based inpainting pipeline that only requires *unconditional* DDPM. In this work, we build a LiDAR completion pipeline by integrating R2DM and RePaint. RePaint involves initializing pixels other than the known ones with Gaussian noise and then carrying out the reverse diffusion process as usual. During this, to harmonize the gap between the known and unknown diffusion extents, reverse and forward processes are repeatedly cycled. In this study, we first change the framework to process on continuous time [14] instead of discrete time [6]. We set the number of sampling steps to 32 and the number of harmonization for each step to 10. Fig. 3 shows some results on various types of corruptions.

IV. EXPERIMENTS

In this section, we report quantitative and qualitative performances of our method on a generation task in Section IV-D and an upsampling tasks in Section IV-E.

A. Settings

To demonstrate the performance on generation and upsampling tasks, we use KITTI-360 datasets. KITTI-360 consists of 81,106 point clouds measured by Velodyne HDL-64E (64-beam LiDAR sensor). The data splits are from Zyrizanov *et al.* [5]. Each of the point clouds is projected to a 64×1024 image. As the baseline, we compare with the state-of-the-art model, LiDARGen¹ [5].

In addition to the diffusion model-based methods, we also compares the GAN-based methods [2]–[4] in the KITTI-Raw benchmark. We employ the data splits and the point clouds projection from the baseline [4]. Note that, in this setting, the point cloud is first projected to a full resolution of 64×2048 and then subsampled to 64×512 .

B. Evaluation metrics

For the generation task, we compute distributional dissimilarity scores between 10k generated samples and all available real data.

1) *Image-based:* Following the baseline [5], we employ Fréchet range distance (FRD) for evaluating generated range and reflectance images. FRD uses the off-the-shelf RangeNet-53 [1] pre-trained a 19-class semantic segmentation task on the SemanticKITTI dataset [27], and calculate the Fréchet distance on the intermediate feature space.

2) *Point clouds-based:* LiDAR range images can be transform back to 3D point clouds. We also evaluate on the level of point clouds with the Fréchet pointcloud distance (FPD) [28]. FPD uses PointNet [29] pre-trained on ShapeNet [30] and calculate the Fréchet distance like FRD.

3) *BEV-based:* Following the baseline [5], we also evaluate on the level of 2D bird’s eye view (BEV) [5] projected from the point clouds. We also compute the Jensen–Shannon divergence (JSD) and minimum matching distance (MMD), which calculate the distance between the marginal distributions of BEV occupancy grids.

C. Implementation details

We used an exponential moving average of model weights to evaluate metrics, with a decay rate of 0.995 per every 10 steps. We performed a distributed training with automatic mixed precision (FP32/FP16) on two NVIDIA A6000 GPUs. Note that we did not use FP16 for LiDARGen to avoid performance degradation. Each model took approximately 34 GPU hours and VRAM 10 GB for training, and 20 GPU hours to generate 10k samples in 1024 denoising steps.

¹We did not borrow the scores on the conference paper [5] but re-evaluate with the officially released samples on <https://github.com/vzyrianov/lidargen>.

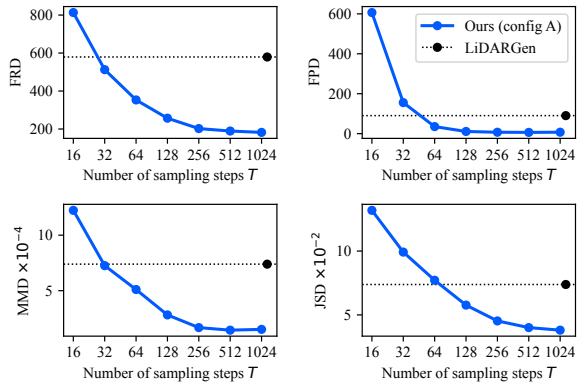


Fig. 4. **Comparison of LiDARGen and ours.** For overall metrics, our method in blue achieved better scores with significantly fewer steps. LiDARGen [5] requires 5×232 steps for sampling.

D. Generation task

In Table II, we list a series of our training configurations (config A–H). The DDPM with config A has closest setup with LiDARGen.

1) *Baselines:* In Fig. 4, we compare LiDARGen and our basic DDPM (config A). For DDPM, we swept the number of sampling steps T in $\{16, 32, 64, 128, 256, 512, 1024\}$. Intuitively, all scores of DDPM improve as T increases. Moreover, our DDPM outperformed LiDARGen with significantly fewer steps. Considering the trade-off between computational time and quality in generation, we will use $T = 256$ for our DDPMs in the following experiments, unless otherwise specified.

2) *Ablations:* Comparing config A and B in Table II, we can see that L_1 loss is not effective for our settings. We attribute the results to that the sample diversity might be degraded, as the similar results were found in natural image domain [31]. We observed that the samples of config B is overly smoothed due to the less sensitivity of L_1 loss. Huber loss (config C), the combination of L_1 and L_2 , showed the marginal improvements only on FRD and MMD. Regarding the representation of range modality, the metric depth (config D) and the inverse depth (config E) improved some metrics, while they harmed FPD. Finally, our model with the coordinates embedding of Fourier features (config H) shows the best results with the large gaps from the other configurations. Without the coordinate embedding (config F), DDPM degrades all the metrics, even worse than the baseline. We hereinafter call config H as R2DM.

3) *Comparison to GANs:* We also compare to the recent GAN-based methods [3, 4] on KITTI-Raw benchmark. With the default setting ($T = 256$), our R2DM could not surpass the latest GAN-based baseline [4]. When increasing the number of timestep T , R2DM outperforms the baseline in FPD. We believe that the performance gap with the KITTI-360 experiment lies in the setup of range images. In KITTI-360 experiments, the range images were downsampled to alleviate missing points called ray-drop noises. In contrast, the range images of KITTI-Raw were also downsampled but the ray-drop noises were retained to be closer to raw data.

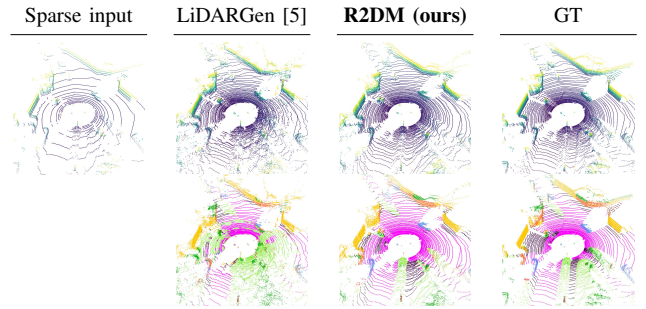


Fig. 5. **Beam-level upsampling results.** We show the point clouds (top) and semantic segmentation results (bottom) predicted by RangeNet-53 [1].

It is considered that there is room for further ingenuity to handle noisy settings, such as full resolution of 64×2048 .

4) *Qualitative results:* Fig. 6 and Fig. 7 show the generated samples of KITTI-360 and KITTI-Raw, respectively. We compare the real data, the baseline, and our method. We can see that our R2DM realizes high consistency in point clouds and the generation of detailed distance values. For instance, regarding the scan lines, our results are less noisy and close to the real data compared to the baselines.

E. Upsampling task

1) *Quantitative results:* Following LiDARGen [5], we conduct $4\times$ upsampling experiment and evaluate point-wise reconstruction performance. We compute mean absolute error (MAE) and root mean squared error (RMSE) for both depth and reflectance modalities. Furthermore, we evaluate semantic consistency between the upsampled results and the ground truths. We used the pre-trained RangeNet-53 [1] used in the FRD evaluation. We calculate intersection-over-union (IoU, %) between the labels predicted from upsampled and ground truth data. The evaluation results are shown in Table IV. Our R2DM outperforms the baselines for all evaluation metrics.

2) *Qualitative results:* We show the upsampling results in Fig. 5. Our methods show better upsampling performance and semantic consistency compared to the baseline.

V. CONCLUSIONS

We proposed R2DM, a denoising diffusion probabilistic model for LiDAR data generation. R2DM can generate realistic LiDAR data as equirectangular images comprising both range and reflectance modalities. Our exploration of effective DDPM designs for the LiDAR domain revealed that geometrical consistency in point clouds is significantly improved by introducing explicit spatial bias through the use of Fourier features. We additionally proposed a completion pipeline that leverages the pre-trained R2DM model. The effectiveness of our approach was demonstrated in two tasks: generation and upsampling. Future work will involve investigating model scalability, developing a noise-robust training method, and extending applications to other perception tasks.

TABLE II
QUANTITATIVE COMPARISON OF KITTI-360 GENERATION.

Method	Framework	T	Configurations			Point cloud	Image	BEV occupancy grid	
			Loss	Range	Coord. embedding	FPD ↓	FRD ↓	MMD $\times 10^4$ ↓	JSD $\times 10^2$ ↓
LiDARGen [5]	NCSNv2	$5 \times 232^\dagger$	L_2	Logarithmic	Identity	90.29	579.39	7.39	7.38
Ours config A	DDPM	256	L_2	Logarithmic	Identity	7.11	202.40	1.67	4.52
config B	DDPM	256	L_1	Logarithmic	Identity	21.42	382.35	7.70	8.28
config C	DDPM	256	Huber	Logarithmic	Identity	11.20	174.83	1.55	4.71
config D	DDPM	256	L_2	Metric	Identity	12.03	229.28	1.47	4.01
config E	DDPM	256	L_2	Inverse	Identity	19.66	188.84	1.85	3.12
config F	DDPM	256	L_2	Logarithmic	w/o embedding	253.21	910.67	40.45	18.05
config G	DDPM	256	L_2	Logarithmic	Spherical harmonics	4.90	180.60	2.18	4.12
config H[‡]	DDPM	256	L_2	Logarithmic	Fourier features	3.92	153.73	0.68	2.17

[†] Five steps for each of the 232 noise levels, which require 1,160 steps in total.

[‡] We call config H as **R2DM** which shows the best performance.

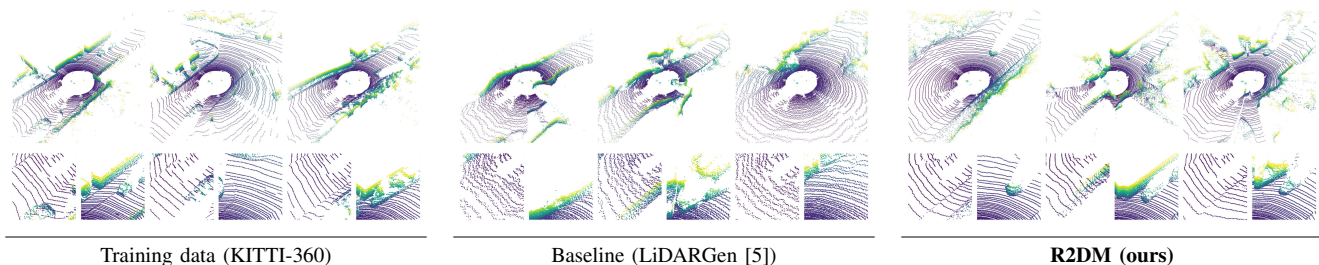


Fig. 6. **Unconditional generation results on KITTI-360.** The baseline results are from officially released samples [5]. Our results are generated with config H in Table II.

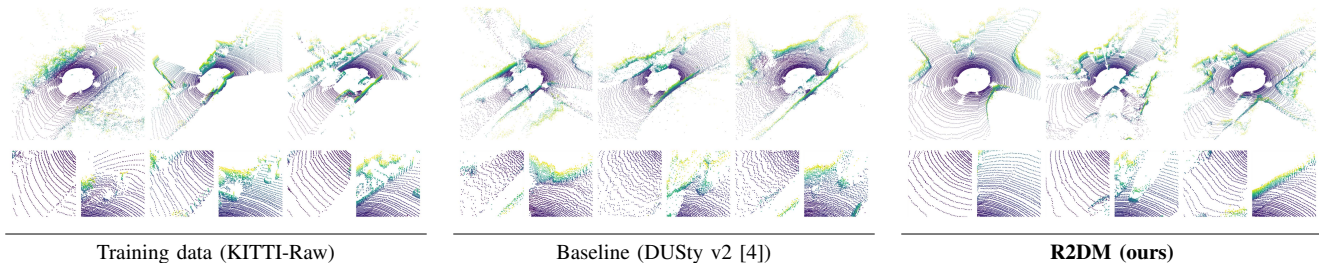


Fig. 7. **Unconditional generation results on KITTI-Raw.** The baseline results are generated using the official pre-trained models [4]. Our results are generated with R2DM ($T = 1024$) in Table III.

TABLE III
QUANTITATIVE COMPARISON ON KITTI-RAW GENERATION.

Method	FRD [†] ↓	FPD ↓	MMD $\times 10^4$ ↓	JSD $\times 10^2$ ↓
Vanilla GAN [2, 3]	N/A	3657.60	1.02	5.03
DUSTy v1 [3]	N/A	223.63	0.80	2.87
DUSTy v2 [4]	N/A	98.02	0.22	2.86
R2DM ($T = 256$)	215.27	128.74	0.72	3.79
R2DM ($T = 512$)	209.24	89.62	0.65	3.76
R2DM ($T = 1024$)	207.31	70.34	0.44	3.56

[†] FRD is not available for the baselines [3, 4] which do not support the reflectance.

TABLE IV
QUANTITATIVE COMPARISON OF $4\times$ UPSAMPLING ON KITTI-360.

Method	Depth		Reflectance		Semantics
	MAE ↓	RMSE ↓	MAE ↓	RMSE ↓	IoU % ↑
Nearest-neighbor	2.069	6.021	0.100	0.169	20.00
Bilinear	2.193	5.432	0.106	0.161	18.19
Bicubic	2.314	5.666	0.110	0.166	17.26
LiDARGen [5]	1.551	5.150	0.080	0.149	22.46
R2DM	0.923	3.911	0.050	0.105	34.44

REFERENCES

- [1] A. Milioto, I. Vizzo, J. Behley, and C. Stachniss, “RangeNet++: Fast and accurate LiDAR semantic segmentation,” in *Proceedings of the IEEE/RSJ International Conference on Intelligent Robots and Systems (IROS)*, 2019, pp. 4213–4220.
- [2] L. Caccia, H. van Hoof, A. Courville, and J. Pineau, “Deep generative modeling of LiDAR data,” in *Proceedings of the IEEE/RSJ International Conference on Intelligent Robots and Systems (IROS)*, 2019, pp. 5034–5040.
- [3] K. Nakashima and R. Kurazume, “Learning to drop points for LiDAR scan synthesis,” in *Proceedings of the IEEE/RSJ International Conference on Intelligent Robots and Systems (IROS)*, 2021, pp. 222–229.
- [4] K. Nakashima, Y. Iwashita, and R. Kurazume, “Generative range imaging for learning scene priors of 3D LiDAR data,” in *Proceedings of the IEEE/CVF Winter Conference on Applications of Computer Vision (WACV)*, 2023, pp. 1256–1266.
- [5] V. Zyrianov, X. Zhu, and S. Wang, “Learning to generate realistic lidar point clouds,” in *Proceedings of the European Conference on*

- Computer Vision (ECCV)*, 2022, pp. 17–35.
- [6] J. Ho, A. Jain, and P. Abbeel, “Denoising diffusion probabilistic models,” in *Proceedings of the Advances in Neural Information Processing Systems (NeurIPS)*, vol. 33, 2020, pp. 6840–6851.
 - [7] C. Saharia, W. Chan, S. Saxena, L. Li, J. Whang, E. L. Denton, K. Ghasemipour, R. Gontijo Lopes, B. Karagol Ayan, T. Salimans *et al.*, “Photorealistic text-to-image diffusion models with deep language understanding,” in *Proceedings of the Advances in Neural Information Processing Systems (NeurIPS)*, vol. 35, 2022, pp. 36479–36494.
 - [8] S. Saxena, A. Kar, M. Norouzi, and D. J. Fleet, “Monocular depth estimation using diffusion models,” 2023.
 - [9] Y. Liao, J. Xie, and A. Geiger, “KITTI-360: A novel dataset and benchmarks for urban scene understanding in 2d and 3d,” *IEEE Transactions on Pattern Analysis and Machine Intelligence (TPAMI)*, vol. 45, no. 3, pp. 3292–3310, 2022.
 - [10] A. Geiger, P. Lenz, C. Stiller, and R. Urtasun, “Vision meets robotics: The KITTI dataset,” *The International Journal of Robotics Research (IJRR)*, vol. 32, no. 11, pp. 1231–1237, 2013.
 - [11] I. Goodfellow, J. Pouget-Abadie, M. Mirza, B. Xu, D. Warde-Farley, S. Ozair, A. Courville, and Y. Bengio, “Generative adversarial nets,” in *Proceedings of the Advances in Neural Information Processing Systems (NeurIPS)*, 2014, pp. 2672–2680.
 - [12] Y. Song and S. Ermon, “Generative modeling by estimating gradients of the data distribution,” in *Proceedings of the Advances in neural information processing systems (NeurIPS)*, 2019, pp. 11895–11907.
 - [13] —, “Improved techniques for training score-based generative models,” in *Proceedings of the Advances in neural information processing systems (NeurIPS)*, vol. 33, 2020, pp. 12438–12448.
 - [14] D. Kingma, T. Salimans, B. Poole, and J. Ho, “Variational diffusion models,” *Proceedings of the Advances in neural information processing systems (NeurIPS)*, vol. 34, pp. 21696–21707, 2021.
 - [15] T. Salimans and J. Ho, “Progressive distillation for fast sampling of diffusion models,” in *Proceedings of the International Conference on Learning Representations (ICLR)*, 2022.
 - [16] R. Xu, X. Wang, K. Chen, B. Zhou, and C. C. Loy, “Positional encoding as spatial inductive bias in gans,” in *Proceedings of the IEEE/CVF Conference on Computer Vision and Pattern Recognition (CVPR)*, 2021, pp. 13569–13578.
 - [17] J. Choi, J. Lee, Y. Jeong, and S. Yoon, “Toward spatially unbiased generative models,” in *Proceedings of the IEEE/CVF International Conference on Computer Vision (ICCV)*, 2021, pp. 14253–14262.
 - [18] D. Verbin, P. Hedman, B. Mildenhall, T. Zickler, J. T. Barron, and P. P. Srinivasan, “Ref-NeRF: Structured view-dependent appearance for neural radiance fields,” in *Proceedings of the IEEE/CVF Conference on Computer Vision and Pattern Recognition (CVPR)*. IEEE, 2022, pp. 5481–5490.
 - [19] K. Zhang, Z. Hong, S. Xu, and S. Wang, “CURL: Continuous, ultra-compact representation for lidar,” in *Proceedings of the Robotics: Science and Systems (RSS)*, 2022.
 - [20] M. Tancik, P. Srinivasan, B. Mildenhall, S. Fridovich-Keil, N. Raghavan, U. Singhal, R. Ramamoorthi, J. Barron, and R. Ng, “Fourier features let networks learn high frequency functions in low dimensional domains,” in *Proceedings of the Advances in Neural Information Processing Systems (NeurIPS)*, vol. 33, 2020, pp. 7537–7547.
 - [21] B. Mildenhall, P. P. Srinivasan, M. Tancik, J. T. Barron, R. Ramamoorthi, and R. Ng, “NeRF: Representing scenes as neural radiance fields for view synthesis,” in *Proceedings of the European Conference on Computer Vision (ECCV)*, 2020, pp. 405–421.
 - [22] P. Dhariwal and A. Nichol, “Diffusion models beat gans on image synthesis,” *Proceedings of the Advances in neural information processing systems (NeurIPS)*, vol. 34, pp. 8780–8794, 2021.
 - [23] K. Nakashima, H. Jung, Y. Oto, Y. Iwashita, R. Kurazume, and O. M. Mozos, “Learning geometric and photometric features from panoramic LiDAR scans for outdoor place categorization,” *Advanced Robotics*, vol. 32, no. 14, pp. 750–765, 2018.
 - [24] S. Schubert, P. Neubert, J. Pöschmann, and P. Protzel, “Circular convolutional neural networks for panoramic images and laser data,” in *Proceedings of the IEEE Intelligent Vehicles Symposium (IV)*, 2019, pp. 653–660.
 - [25] G. Lin, A. Milan, C. Shen, and I. Reid, “Refinenet: Multi-path refinement networks for high-resolution semantic segmentation,” in *Proceedings of the IEEE/CVF Conference on Computer Vision and Pattern Recognition (CVPR)*, 2017, pp. 1925–1934.
 - [26] A. Lugmayr, M. Danelljan, A. Romero, F. Yu, R. Timofte, and L. Van Gool, “RePaint: Inpainting using denoising diffusion probabilistic models,” in *Proceedings of the IEEE/CVF Conference on Computer Vision and Pattern Recognition (CVPR)*, 2022, pp. 11461–11471.
 - [27] J. Behley, M. Garbade, A. Milioto, J. Quenzel, S. Behnke, C. Stachniss, and J. Gall, “SemanticKITTI: A dataset for semantic scene understanding of LiDAR sequences,” in *Proceedings of the IEEE/CVF International Conference on Computer Vision (ICCV)*, 2019.
 - [28] D. W. Shu, S. W. Park, and J. Kwon, “3d point cloud generative adversarial network based on tree structured graph convolutions,” in *Proceedings of the IEEE/CVF International Conference on Computer Vision (ICCV)*, 2019.
 - [29] C. R. Qi, H. Su, K. Mo, and L. J. Guibas, “PointNet: Deep learning on point sets for 3d classification and segmentation,” in *Proceedings of the IEEE Conference on Computer Vision and Pattern Recognition (CVPR)*, 2017.
 - [30] A. X. Chang, T. Funkhouser, L. Guibas, P. Hanrahan, Q. Huang, Z. Li, S. Savarese, M. Savva, S. Song, H. Su, J. Xiao, L. Yi, and F. Yu, “ShapeNet: An information-rich 3D model repository,” Tech. Rep., 2015.
 - [31] C. Saharia, W. Chan, H. Chang, C. Lee, J. Ho, T. Salimans, D. Fleet, and M. Norouzi, “Palette: Image-to-image diffusion models,” in *ACM SIGGRAPH 2022 Conference Proceedings*, 2022, pp. 1–10.